Determination of K_S^0 fragmentation functions including BESIII measurements and using neural networks

Maryam Soleymaninia[1,*], Hadi Hashamipour,[2,1,†] Maral Salajegheh[3,‡] Hamzeh Khanpour[4,5,1,§]
Hubert Spiesberger[6,‖] and Ulf-G. Meißner[3,7,8,¶]

[1]*School of Particles and Accelerators,
Institute for Research in Fundamental Sciences (IPM), P.O.Box 19395-5531, Tehran, Iran*
[2]*Istituto Nazionale di Fisica Nucleare, Gruppo collegato di Cosenza,
I-87036 Arcavacata di Rende, Cosenza, Italy*
[3]*Helmholtz-Institut für Strahlen-und Kernphysik and Bethe Center for Theoretical Physics,
Universität Bonn, D-53115 Bonn, Germany*
[4]*AGH University, Faculty of Physics and Applied Computer Science, Al. Mickiewicza 30,
30-055 Kraków, Poland*
[5]*Department of Physics, University of Science and Technology of Mazandaran,
P.O.Box 48518-78195, Behshahr, Iran*
[6]*PRISMA⁺ Cluster of Excellence, Institut für Physik,
Johannes-Gutenberg-Universität, Staudinger Weg 7, D-55099 Mainz, Germany*
[7]*Institute for Advanced Simulation (IAS-4), Forschungszentrum Jülich, D-52425 Jülich, Germany*
[8]*Tbilisi State University, 0186 Tbilisi, Georgia*

In this study, we revisit the extraction of parton-to-K_S^0 hadron fragmentation functions, named FF24-K_S^0, focusing on both next-to-leading-order and next-to-next-to-leading-order accuracy in perturbative QCD. Our approach involves the analysis of single inclusive electron-positron annihilation (SIA) data. The two key improvements are, on the one hand, the incorporation of the latest experimental data from the BESIII experiment and, on the other hand, the adoption of neural networks in the fitting procedure. To address experimental uncertainties, the Monte Carlo method is employed. Our investigation also explores the impact of hadron mass corrections on the description of SIA data, spanning a broad kinematic regime with a particular emphasis on the range of small z values. The theory prediction for K_S^0 production at both NLO and NNLO accuracy exhibits good agreement with experimental data within their respective uncertainties.

I. INTRODUCTION

Fragmentation functions (FFs) play a crucial role in the computation of scattering cross sections that involve detected final-state hadrons. When there is a high energy scale, QCD factorization allows us to disentangle the physics of a parton transitioning to a colorless hadron from the hard scattering process that generated the parton [1].

[*]Contact author: Maryam_Soleymaninia@ipm.ir
[†]Contact author: hadi.hashamipour@lnf.infn.it
[‡]Contact author: Maral@hiskp.uni-bonn.de
[§]Contact author: Hamzeh.Khanpour@cern.ch
[‖]Contact author: spiesber@uni-mainz.de
[¶]Contact author: meissner@hiskp.uni-bonn.de

Parton-to-hadron FFs precisely depict this transition and illustrate how QCD final states are nonperturbatively created through hadronization, providing insight into the dynamics of the strong interaction. Fragmentation functions are process-independent quantities and can be determined from data through a comprehensive QCD analysis. The variation of the FFs with energy can be perturbatively calculated, comprising an expansion in the strong coupling, and is presently understood up to next-to-next-to-leading order (NNLO) accuracy [2,3]. Due to the significance of FFs, there has been considerable theoretical attention toward their global analysis, resulting in the development of multiple new sets for various hadron FFs [4–7].

Fragmentation functions have a large diversity of applications. Their knowledge is essential in numerous hard scattering processes at both existing and upcoming experiments, such as at the Large Hadron Collider (LHC), the Future Circular Collider (FCC) [8,9], and the Electron-Ion Collider (EIC) [10]. Particle production measurements provide valuable insight into the dynamics of QCD

interactions at low momentum transfer. Accurate modeling of these interactions is crucial for understanding and constraining the impact of the underlying event in collisions at high transverse momentum investigated at the LHC. Other applications include the examination of the spin structure of the nucleon [11]. Moreover, FFs play a pivotal role in investigating hadron production rates in scattering processess involving heavy nuclei [12].

The distribution of hadrons containing strange quarks has been documented at various center-of-mass energies, both at the LHC [13,14] and at the Tevatron [15]. Kaons are particularly important. FFs for K_S^0 production have been calculated by some of the authors of the present paper [16], denoted SAK20. Other research groups, such as BKK96 [17], BS [18], AKK05 [19], AKK08 [20], DSS17 [21], and NNFF [22] have also investigated K_S^0 FFs. Details of these analyses are discussed elsewhere, and we direct the reader to our previous paper [16] for a review.

In our previous investigations, referred to as SAK20, we incorporated experimental data from the single inclusive electron-positron annihilation process (SIA) to determine FFs for K_S^0 production. We provided FF sets for K_S^0, along with their associated uncertainties determined through the Hessian method, at both next-to-leading order (NLO) and NNLO precision. Additionally, in [16] we had examined the effect of hadron mass corrections as well.

Recently, the BESIII detector has performed measurements of the normalized differential cross sections for inclusive K_S^0 production in e^+e^- annihilation, covering six energies from 2.2324 to 3.6710 GeV with relative hadron energies, z, ranging from 0.2 to 0.9 [23]. Since this energy range is not well covered by previous experimental data, it will provide valuable input for a QCD analysis to determine the kaon FFs. This new dataset motivates us to revisit and update our previous analysis of K_S^0 FFs [16], now incorporating the BESIII measurements. Our new FF sets, FF24-K_S^0, at both NLO and NNLO, are publicly available in the LHAPDF format.

In recent years, machine learning (ML) has gained increasing popularity in various domains of particle physics, particularly in collider physics. One promising application of ML methods is their role in advancing our understanding of nonperturbative quantities related to nucleons, such as parton distribution functions (PDFs) and FFs [22,24,25]. Given this trend, we chose to leverage artificial neural networks (NN) for the extraction of FFs for K_S^0 hadrons in this work. Utilizing neural networks is expected to minimize the bias in the parametrization of the FFs. In addition, we use the Monte Carlo sampling method as a robust statistical approach to account for uncertainties in experimental data and derive probability density distributions of FFs from the data. To facilitate this analysis, we utilize the publicly available code MONTBLANC, accessible from [26].

The organization of this paper is as follows: In Sec. II we present and discuss the experimental observable for K_S^0 production in the SIA process. The theoretical framework employed in this work as well as the hadron mass corrections are presented in Sec. III. Section IV deals with the χ^2 minimization and the methodology for the calculation of FFs uncertainties. Our main results from this study are presented and discussed in detail in Sec. V. Finally, Sec. VI provides our summary and conclusions.

II. EXPERIMENTAL DATA

This analysis relies on experimental measurements of the K_S^0 production cross sections in the SIA process. Various collaborations have reported SIA data for the cross section of K_S^0 hadrons in the final state, considering the longitudinal momentum fraction z at different energy scales. The majority of differential cross sections have been normalized to the total cross section.

In this analysis, we incorporate a comprehensive set of experimental data from various collaborations conducted at CERN, DESY, SLAC, KEK, and BESIII. Our dataset encompasses untagged data from the TASSO collaboration at $\sqrt{s} = 14$, 22, and 34 GeV [27], as well as at $\sqrt{s} = 14.8$, 21.5, 34.5, 35, and 42.6 GeV [28]. Additionally, we include measurements from the HRS [29], TPC [30], and MARK II [31] collaborations at $\sqrt{s} = 29$ GeV. Our dataset also includes data from the CELLO collaboration at $\sqrt{s} = 35$ GeV [32] and the TOPAZ collaboration at $\sqrt{s} = 58$ GeV [33].

Included in our analysis are also datasets measured at $\sqrt{s} = M_Z$ from ALEPH [34], DELPHI [35], and OPAL [36], as well as untagged and tagged quark data (light quarks (u, d, s) and heavy quarks c and b) from the SLD [37] collaboration.

The primary motivation for this analysis is the incorporation of the most recent measurements of normalized differential cross sections for inclusive K_S^0 production in SIA processes reported by the BESIII collaboration [23]. Their dataset spans six center-of-mass energies ranging from $\sqrt{s} = 2.2324$ to 3.6710 GeV and features a z coverage from 0.2 to 0.9. Collected with the BESIII detector at BEPCII, these new measurements offer crucial input for fitting FFs in the region with $\sqrt{s} < 10$ GeV, where precision SIA data have been scarce.

As Fig. 3 of the BESIII publication [23] shows, the comparison between the K_S^0 data and different theoretical predictions indicates a discrepancy, likely attributed to the fact that existing FFs had been determined from SIA data at high energies and have to be extrapolated to the lower energy scales of the BESIII measurement. One can conclude that BESIII data should be used to improve the fits of FFs at the low energy scales.

Kinematic cuts are implemented to ensure that the selected data points are in a regime where perturbative
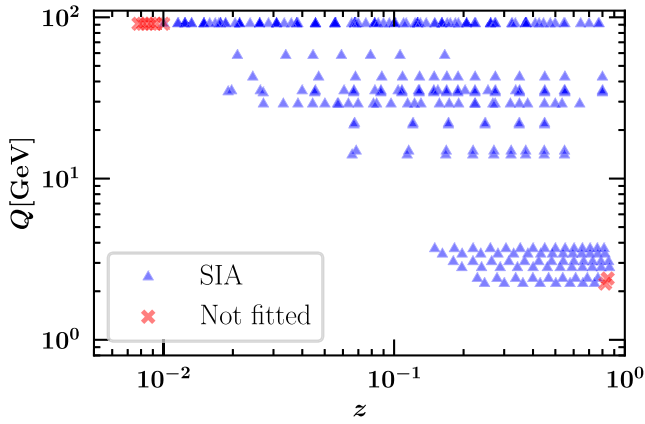
FIG. 1.   Kinematic range of the experimental SIA data in the (z, Q) plane used to determine the K_S^0 FFs.

fixed-order predictions hold reliable. The kinematic coverage of the datasets applied in this analysis is shown in Fig. 1. We adjust the minimal value of z at $z_{\min} = 0.013$ for all experiments. For most of the experiments, the upper limit $z_{\max}$ is set at 0.9, except for two datasets from BESIII: the data at the energies $\sqrt{s} = 2.2324$ and 2.4 GeV are cut at $z_{\max} = 0.8$. Due to outliers observed in the final data points of these datasets, their inclusion in the fit leads to an increased χ^2 value without substantially altering the resulting FFs. Hence, there is no compelling rationale for integrating them into the analysis. Overall, we omit just 8 data points across all the SIA datasets used in this analysis and find that $N_{\mathrm{dat}} = 346$ data points can be used.

It is worth mentioning that, unlike in our previous analysis [16], we chose not to incorporate the experimental data from HRS [29] and DELPHI at 183 and 189 GeV [38] in this study. This decision was made since we could not find a satisfactory fit for these particular datasets. Specifically, their inclusion resulted in a noticeable decline in the overall quality of the fit, with χ^2 values per data point exceeding 7 for HRS, approximately 7 for DELPHI at 183 GeV, and surpassing 17 at 189 GeV. This discrepancy is evident when comparing the high χ^2 values per data point observed in our previous analysis and in AKK08 [20] to the even poorer performance in the current analysis. We have identified the source of this discrepancy as an apparent inconsistency between these three datasets and the others, particularly with BESIII.

III. THEORETICAL SETUP

The theoretical setup of our analysis closely follows that illustrated in Sec. III of Ref. [16]. In this section, we recapitulate the theoretical understanding of standard collinear factorization, comprising perturbative and non-perturbative components of the cross section for the SIA process. We also review the timelike DGLAP evolution of FFs, alongside detailing numerical computations of SIA

cross-sections, including theoretical settings and physical parameters.

The total cross section for e^+e^- annihilation in the production of hadrons ($e^+e^- \to h + X$) can be expressed in terms of the convolution of coefficient functions and FFs

$$\frac{1}{\sigma_{\mathrm{tot}}}\frac{d\sigma^h}{dz} = \frac{1}{\sigma_{\mathrm{tot}}} C_i\left(x, \alpha_s(\mu), \frac{Q^2}{\mu^2}\right) \otimes D_i^h\left(\frac{z}{x}, \mu^2\right). \quad (1)$$

The coefficient functions $C_i(x, \alpha_s(\mu), Q^2/\mu^2)$ are currently computed up to $\mathcal{O}(\alpha_s^2)$ in perturbative QCD [3,39] and $D_i^h(z/x, \mu^2)$ denotes the FFs. The parton FFs at different energy scales are connected through the timelike DGLAP evolution equations [40], given by

$$\frac{\partial D_i^h(z, \mu^2)}{\partial \ln \mu^2} = P_{ji}(x, \alpha_s(\mu^2)) \otimes D_j^h\left(\frac{z}{x}, \mu^2\right). \quad (2)$$

In this equation, $P_{ji}(x, \alpha_s(\mu^2))$ represent the timelike splitting functions and $\otimes$ denotes the convolution integral.

When incorporating the mass of the produced hadrons into the kinematic calculations, hadron mass corrections modify the FFs. In the context of the SIA process, these corrections are very large and therefore indispensable, in particular at low values of z. Hadron mass effects are introduced by employing light-cone coordinates and can be taken into account by using a modified scaling variable η instead of z

$$\eta = \frac{z}{2}\left(1 + \sqrt{1 - \frac{4m_h^2}{sz^2}}\right), \quad (3)$$

where m_h is the hadron mass. With this change of variables we can express the cross section as

$$\frac{d\sigma}{dz} = \frac{1}{1 - m_h^2/s\eta^2} \sum_a \int_\eta^1 \frac{dx_a}{x_a} \frac{d\hat{\sigma}_a}{dx_a} D_a^h\left(\frac{\eta}{x_a}, \mu\right), \quad (4)$$

Here, $d\hat{\sigma}_a/dx_a$ denotes the differential cross section of the hard subprocess with parton a, calculated in pQCD, and a runs over all quark flavors and the gluon. We use Eq. (4) for the theory predictions of this work. In this study, we compute the K_S^0 hadron FFs within the framework of the zero-mass variable-flavor-number scheme (ZM-VFNS), where all active flavors are treated as massless. However, the inclusion of heavy quark masses is necessary in order to calculate the number of active flavors taking into account the correct heavy-quark thresholds.

In this analysis, fixed values are adopted for the charm and bottom quark masses, setting $m_c = 1.51$ GeV and $m_b = 4.92$ GeV, respectively. The strong running coupling is calculated at two-loop order by setting $\alpha_s(m_Z = 91.1876 \text{ GeV}) = 0.118$.
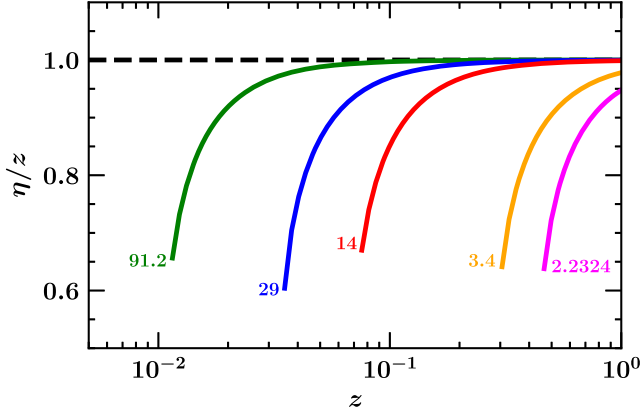
FIG. 2. Ratio η/z as a function of z at five representative values of $\sqrt{s}$.

To illustrate the need for hadron mass corrections, we present in Fig. 2 the ratio η/z as a function of z at five representative values of $\sqrt{s}$. This figure indicates that the deviation of the momentum fraction available to the hadron (η) from z becomes significant when z and/or $\sqrt{s}$ decrease. We see that at $\sqrt{s} = 2.2324$ GeV and $\sqrt{s} = 3.4$ GeV this correction is sizeable in the full range of z values. The corrections are larger than 20% for $z < 0.6$ at $\sqrt{s} = 2.2324$ GeV, $z < 0.3$ at $\sqrt{s} = 3.4$ GeV, $z < 0.1$ at $\sqrt{s} = 14$ GeV, $z < 0.04$ at $\sqrt{s} = 29$ GeV, and $z < 0.015$ at $\sqrt{s} = 91.2$ GeV. Corrections exceeding 50% can be observed around $z < 0.4$ at $\sqrt{s} = 2.2324$ GeV, $z < 0.3$ at $\sqrt{s} = 3.44$ GeV, $z < 0.06$ at $\sqrt{s} = 14$ GeV, $z < 0.03$ at $\sqrt{s} = 29$ GeV, and $z < 0.01$ at $\sqrt{s} = 91.2$ GeV. Since we include the new BESIII data, which have been measured from 2.2324 to 3.6710 GeV, the hadron mass corrections are essential in the kinematic region covered by the data and significantly improves the description of the data used in this analysis.

For the cross sections, Eq. (4), our investigations show that at the energy scale of 91.2 GeV, the hadron mass correction is approximately $\pm 4\%$. At lower values of $\sqrt{s} = 29$ GeV, relevant for the TPC data, this correction varies approximately in the range between $\sim -20\%$ and $\sim +6\%$ depending on the value of z, while for the case of the TASSO 14 data, the correction is between -20% and $+12\%$. Our finding is that for energies of 3.4 GeV and 2.2324 GeV, mass corrections become more important and reach $\sim \pm 45\%$ at $\sqrt{s} = 3.4$ GeV and $\sim +35\%$ to $\sim -50\%$ at $\sqrt{s} = 2.2324$ GeV for BESIII. All in all, hadron mass corrections prove to be significant in mid-range energies and indispensable for low-energy experiments conducted at BESIII.

As outlined in our previous publication [16], the analysis of inclusive SIA data only allows one to determine the combined quark and antiquark FFs, i.e., for the quark combinations $q^+ = q + \bar{q}$. SIA cross section data are available for tagged light, charm, and bottom quarks.

Therefore we can adopt a flavor decomposition approach and, keeping in mind the flavor content of K_S^0, we chose the following combinations to be fitted:

$$D_{u^+}^{K_S^0}, \quad D_{d^+}^{K_S^0}, \quad D_{s^+}^{K_S^0}, \quad D_{c^+}^{K_S^0}, \quad D_{b^+}^{K_S^0}, \quad D_{g}^{K_S^0}. \quad (5)$$

In the next section we describe the optimization methodology and the method of FFs determination.

IV. OPTIMIZATION METHODOLOGY AND UNCERTAINTY

The determination of unknown parameters or functions typically involves employing a maximum log-likelihood method. Assuming small uncertainties and therefore an approximately linear parameter dependence, the problem can be reduced to minimizing an appropriately chosen χ^2. In this work we use neural networks to describe the theoretical predictions and choose to minimize the following χ^2 function:

$$\chi^{2(k)} \equiv (\mathbf{T}(\boldsymbol{\theta}^{(k)}) - \boldsymbol{x}^{(k)})^{\mathrm{T}} \cdot \mathbf{C}^{-1} \cdot (\mathbf{T}(\boldsymbol{\theta}^{(k)}) - \boldsymbol{x}^{(k)}). \quad (6)$$

Here, k is the replica number, $\boldsymbol{x}^{(k)}$ denotes pseudodata for replica k which are obtained by randomly shifting the central values proportional to their uncertainties, and $\boldsymbol{\theta}$ represents the set of weights and biases in the neural network, $\mathbf{C}$ represents the covariance matrix including all uncertainties and (possible) correlations of the measured data $\boldsymbol{x}$, and finally $\mathbf{T}$ represents the theoretical prediction. We use the open source framework MONTBLANC in all the analyses performed in this work. In this framework, minimization of χ^2 is performed by the CERES SOLVER open source code [41]. The NN parametrization is provided by the NNAD code [42]. The core of our theoretical predictions relies on the APFEL++ package [43]. Using NNAD an analytic expression for χ^2 is formed and CERES SOLVER is used to solve the corresponding minimization problem using trust region methods. The FFs for each parton flavor are expressed through a NN model at the initial scale $Q_0 = 5$ GeV as

$$zD_i^{h^+}(z, Q_0) = (N_i(z; \boldsymbol{\theta}) - N_i(1; \boldsymbol{\theta}))^2. \quad (7)$$

$N_i(z; \boldsymbol{\theta})$ denotes the output generated by the neural network. We opt not to incorporate prefactors like $z^\alpha (1 - z)^\beta$ to regulate the behavior at low and high values of z. However, it is important to note that the NN output is subtracted at $z = 1$, ensuring that the fragmentation functions vanish at this specific kinematic point. Moreover, the resulting output is squared to guarantee that FFs remain non-negative.

The neural network is a type of multi-layer feed-forward perceptron [44]. It comprises nodes organized into sequential layers, where the output $\xi_i^{(l)}$ of the i-th node in the l-th layer is,

$$\xi_i^{(l)} = g\left(\sum_j \omega_{ij}^{(l)} \xi_j^{(l-1)} + \theta_i^{(l)}\right). \qquad (8)$$

The function g is called *activation function*, which is a sigmoid function for hidden layers and linear for the output layer. The parameters $\{\omega_{ij}^{(l)}, \theta_i^{(l)}\}$, denote *weights* and *biases* respectively, and are determined by minimization of the χ^2 function.

We use a simple but effective method in this study. Its effectiveness is based on the so-called universal approximation theorem [45], which states that a simple feed-forward NN like the one we are using can represent any function in any specified range. Our NN setup has just one hidden layer, and we pick 25 nodes for it. We have one node in the input layer, which is the value of z, and 6 output nodes, one for each combination of FFs in Eq. (5). This architecture is therefore denoted as (1-25-6) and has 175 weight and 31 bias parameters, i.e., 206 parameters in total to be fitted to the data. Fewer nodes could work just as well. We have tried a NN setup with two hidden layers, (1-9-9-6), to see if this would change our results. Unsurprisingly, our tests showed that the results are consistent, as other research supports this idea [46].

We use cross-validation to avoid overfitting our FFs. For each data replica, the datasets with more than 10 points are randomly split into training and validation subsets, each containing half of the points. We only use the training group to perform the fit. If there are 10 or fewer points, we use all of them for training. During the training step, the χ^2-value of the validation set is monitored. The fit is stopped when χ^2 of the validation set reaches its minimum. Replicas whose total χ^2 per point is larger than three are discarded. We are therefore convinced that our results do indeed describe the data, rather than the specific setup of the NN. Finally, we decided to use 100 replicas for our analysis, as it was shown in a previous study to be enough to represent the central values and uncertainties of the FFs [47].

The Monte Carlo approach has become a prevalent technique in various QCD analyses for error propagation, as evidenced by its application in studies such as [25,48–51]. Here, this method involves estimating the posterior probability distribution of NN parameters through fitting multiple times. Each fit is conducted independently using a pseudo dataset, known as a replica, resulting in an optimal set of parameters and therefore FFs. Subsequently, the results of all fits collectively encapsulate the probability distribution of the data in FFs. Therefore, we define both the central value as the mean of the replicas, and the uncertainties of FFs as the standard deviation over the replica set.

V. RESULTS AND DISCUSSION

The main results and findings of this study are presented and discussed in detail in this section. First, we evaluate the quality of the FF24-K_S^0 fit by examining the total and individual values of χ^2 per dataset. Second, we perform a comparison between the analyzed experimental data and the predictions obtained using our K_S^0 FFs for all the datasets included in this analysis. The kinematical cuts are also discussed in this section. Finally, we compare our FFs with other determinations available in the literature and illustrate the origin of some specific features of our new FFs.

The experimental data used in this analysis are collected in Table I. The table includes the reference for each dataset and the associated energy scale. Additionally, details about the kinematic cuts for both small and large regions of z are provided. The last two columns show the χ^2 values per data point for each dataset at both NLO and NNLO accuracy. The table also presents the total χ^2 values for all the SIA datasets.

The analysis includes a total of 346 data points after the application of the kinematical cuts described above. The overall χ^2 per data point is 0.91 for the NLO and 0.87 for the NNLO analysis, showcasing a highly effective description of the entire dataset for both perturbative orders.

A detailed examination of the entries in Table I reveals a consistent fit quality and satisfactory description for each individual dataset. It is noteworthy that the incorporation of NNLO corrections results in a reduction of χ^2 per data point for most of the datasets, contributing to a further enhancement of the overall fitting quality indicated by the total χ^2.

In the following, we compare the theoretical predictions calculated using the FF24-K_S^0 FFs with the analyzed experimental data for all the datasets, focusing on NNLO accuracy. In Figs. 3, 4, and 5, we present the predictions for the normalized differential cross section at NNLO accuracy as a function of z, compared with the SIA data. The upper panels of the figures show the actual cross sections from experiment (black points) and theory (red points). In the lower panels of Figs. 3–5, the black points show the ratios of data over theory for each dataset, allowing for a better comparison of the central values of our theoretical predictions at NNLO accuracy with experimental data. The error bars of the black (red) points are obtained by normalizing the experimental (theoretical) uncertainties to the central values of our theory prediction.

Some of the data points have been excluded from the fits, as explained earlier. In the figures, these points are separated by a blue dotted line. Specifically, we have omitted two data points from ALEPH and four data points from DELPHI in the small z region due to their tension with the rest of the data. Additionally, we observed outliers in the last data points of BESIII2.2324 and BESIII2.4, which deviate from the overall trend. Consequently, we decided to exclude them from our analysis as well. All data points from the remaining datasets are included in our analysis. The χ^2 values listed in Table I demonstrate that our predictions are in good agreement with the data. A detailed comparison of the K_S^0 production cross section calculated at NNLO accuracy and the newly added BESIII data are presented

TABLE I. The list of input datasets included in the analysis of K_S^0 FFs at NLO and NNLO accuracy. For each dataset, we provide the name of the experiment, the corresponding published reference, the center-of-mass energy $\sqrt{s}$, and the value of χ^2 per data point for the individual dataset at NLO and NNLO accuracy. The total value of χ^2 per data point is shown in the last line.

Experiment	Reference	$\sqrt{s}$ GeV	z_{min}	z_{max}	χ^2_{NLO}/#data	χ^2_{NNLO}/#data
BESIII	[23]	2.2324	0.013	0.8	0.92	0.94
BESIII	[23]	2.4	0.013	0.8	0.14	0.20
BESIII	[23]	2.8	0.013	0.9	2.55	2.18
BESIII	[23]	3.05	0.013	0.9	1.37	1.39
BESIII	[23]	3.4	0.013	0.9	0.84	0.85
BESIII	[23]	3.6710	0.013	0.9	0.55	0.56
TASSO	[27]	14	0.013	0.9	0.68	0.63
TASSO	[28]	14.8	0.013	0.9	1.60	1.55
TASSO	[28]	21.5	0.013	0.9	1.19	1.07
TASSO	[27]	22	0.013	0.9	1.27	1.17
TPC	[30]	29	0.013	0.9	0.23	0.22
MARKII	[31]	29	0.013	0.9	0.37	0.33
TASSO	[27]	34	0.013	0.9	2.04	1.83
TASSO	[28]	34.5	0.013	0.9	1.27	1.21
TASSO	[28]	35	0.013	0.9	0.92	0.85
CELLO	[32]	35	0.013	0.9	0.40	0.35
TASSO	[28]	42.6	0.013	0.9	1.19	1.15
TOPAZ	[33]	58	0.013	0.9	0.34	0.32
ALEPH	[34]	91.2	0.013	0.9	0.35	0.32
DELPHI	[35]	91.2	0.013	0.9	0.70	0.73
OPAL	[36]	91.2	0.013	0.9	0.90	0.88
SLD total	[37]	91.2	0.013	0.9	0.93	0.93
SLD uds	[37]	91.2	0.013	0.9	0.65	0.73
SLD charm	[37]	91.2	0.013	0.9	0.64	0.66
SLD bottom	[37]	91.2	0.013	0.9	1.64	1.46
			Total #data			
Total χ^2/#data					346 0.91	0.87

in Fig. 5. As can clearly be seen, very nice agreement is achieved, which is consistent with the χ^2 values presented in Table I. The incorporation of BESIII data contributes significantly to the precision and reliability of our new NNLO FF set.

It is worth noting that when datasets are consistent with each other, one would typically expect the predictions to have uncertainties of a similar magnitude as those of the experimental data. However, if there are inconsistencies in the data, uncertainties may decrease to account for this discrepancy. This phenomenon, where the combination of multiple datasets leads to a reduction in the overall uncertainty, is evident in Figs. 3, 4, and 5. Similar observations can be made in Fig. 2 of [24] and in our previous analysis using MONTBLANC [4].

Now we present our K_S^0 FFs, denoted as FF24-K_S^0, obtained from our baseline NLO and NNLO QCD fits and compare them with some other FF parametrizations available in the literature. Such comparisons are shown in Figs. 6 and 7. For the NLO analysis, we compare with SAK20 [16], AKK08 [20], and DSS17 [21]. Results from SAK20 [16] and NNFF1.0 [22] are compared with our NNLO fit results.

All four FF sets depicted in Fig. 6 include a comparable array of SIA datasets. However, our new FF24-K_S^0 set uniquely integrates the BESIII measurements for the first time. Additionally, the AKK08 FF encompasses K_S^0 hadron production measurements from $pp(\bar{p})$ collisions. With the exception of DSS17, hadron mass corrections are accounted for in the other three FF sets. Both the FF24-K_S^0 and SAK20 FFs are computed up to NNLO accuracy. In contrast, the AKK08 FFs are determined only up to NLO accuracy and available only without an uncertainty estimate. DSS17 [21] also presented their FFs at NLO accuracy along with uncertainty bands extracted from SIA, lepton-nucleon DIS, and proton-proton collision data. The minimum value for z is considered to be 0.05 in both the SAK20 and AKK08 analyses. However, in the FF24-K_S^0 analysis, we incorporated data points also for smaller z, down to $z \geq 0.013$. This difference could result in some variations among the four FF analyses for all flavors, in particular in the small-z region, $z < 0.05$.
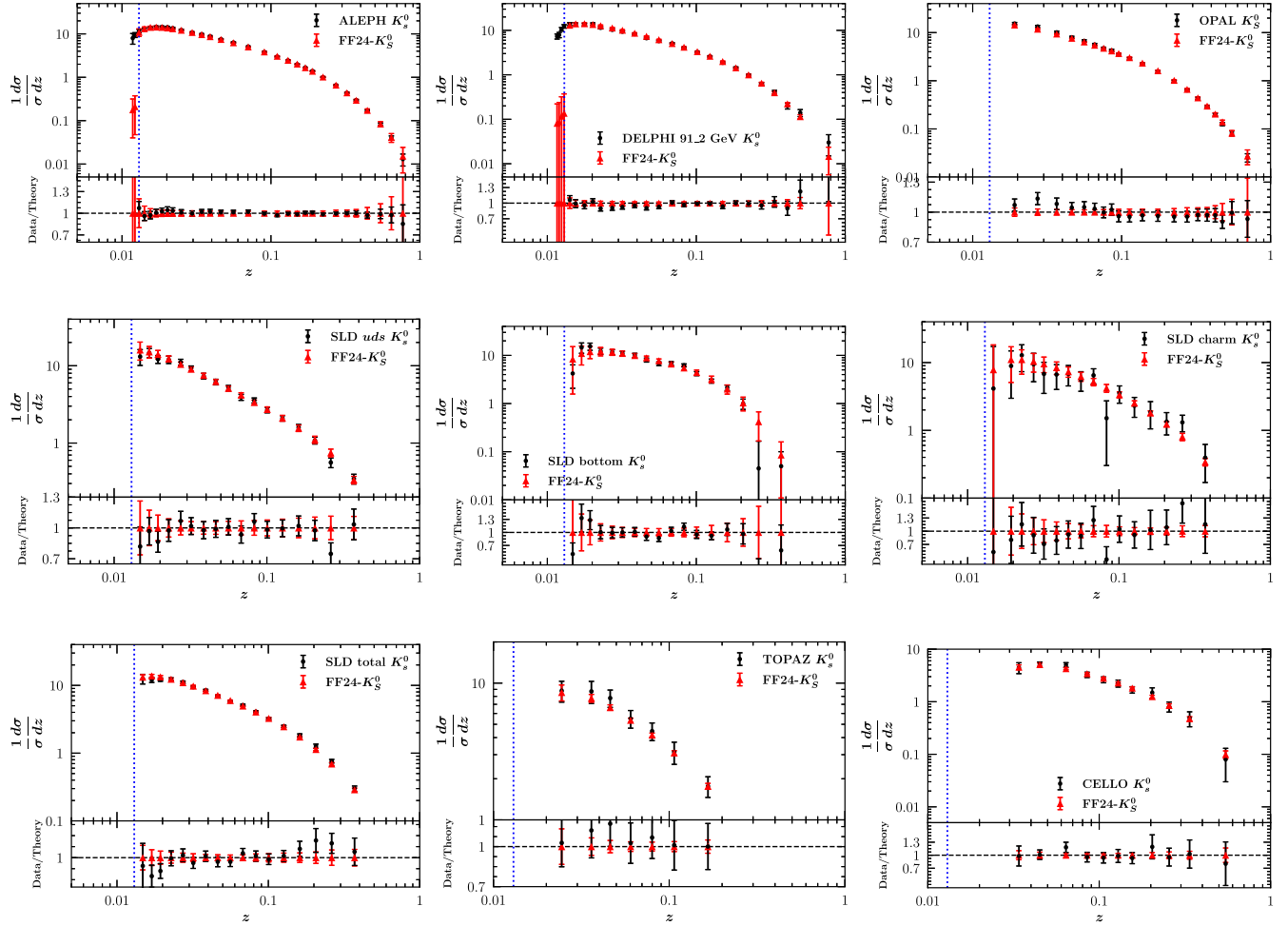
FIG. 3.   Comparison between the K_S^0 production cross section calculated at NNLO accuracy and experimental data from different experiments, including ALEPH, DELPHI91.2, OPAL, SLD$_{uds}$, SLD$_b$, SLD$_c$, SLD$_{total}$, TOPAZ, and CELLO. The lower panels show the data/theory ratios.

Considering the comparisons presented in Fig. 6, several observations are noteworthy. It is evident that the central values of these analyses exhibit different behaviors, particularly for the gluon and u^+ FFs, even within regions defined by the same kinematical cuts. Despite these differences, some similarities emerge, such as at large z values for the b^+, c^+, s^+, and d^+ FFs. In the small z region, where more data points are included in the FF24-K_S^0 analysis, the FFs are generally larger than those of the SAK20 FF, except for the gluon FF.

Regarding uncertainty bands, there are some comments need to be made as well. As shown in Fig. 6, the uncertainty bands for FF24-K_S^0 FFs are broader compared to those of the SAK20 analysis across nearly all the z region. This difference primarily arises from our utilization of the Monte Carlo method to accommodate error bands, whereas the SAK20 analysis employs the standard Hessian method. Notably, the uncertainty bands for the new FF24-K_S^0 FFs are wide over regions at small values of z due to the

insufficient coverage of SIA data points in those areas. These wide uncertainty bands are particularly pronounced for the u^+ and s^+ FFs. Upon comparison with DSS17, it becomes evident that their analysis yields larger error bands across nearly all FFs, except for the d^+ FFs.

We now shift our focus to the comparison of the FF24-K_S^0 at NNLO accuracy with those of SAK20 [16] and NNFF1.0 [22]. These comparisons are illustrated in Fig. 7. Considering the central values of these analyses, one can observe different behaviors for all parton species, even within regions defined by the same kinematical cuts. For the case of b^+, c^+, and s^+ FFs, the central values of FF24-K_S^0 are smaller than those of SAK20 [16] and NNFF1.0 [22]. However, for the u^+ and gluon FFs, although they are larger in comparison to SAK20, they are still smaller than those of NNFF1.0. In terms of uncertainty bands, it is noticeable that the error bands of FF24-K_S^0 are smaller than those of NNFF1.0 for almost all parton species and across all regions of z, particularly for the small-z region $z < 0.1$. When comparing with SAK20, it can
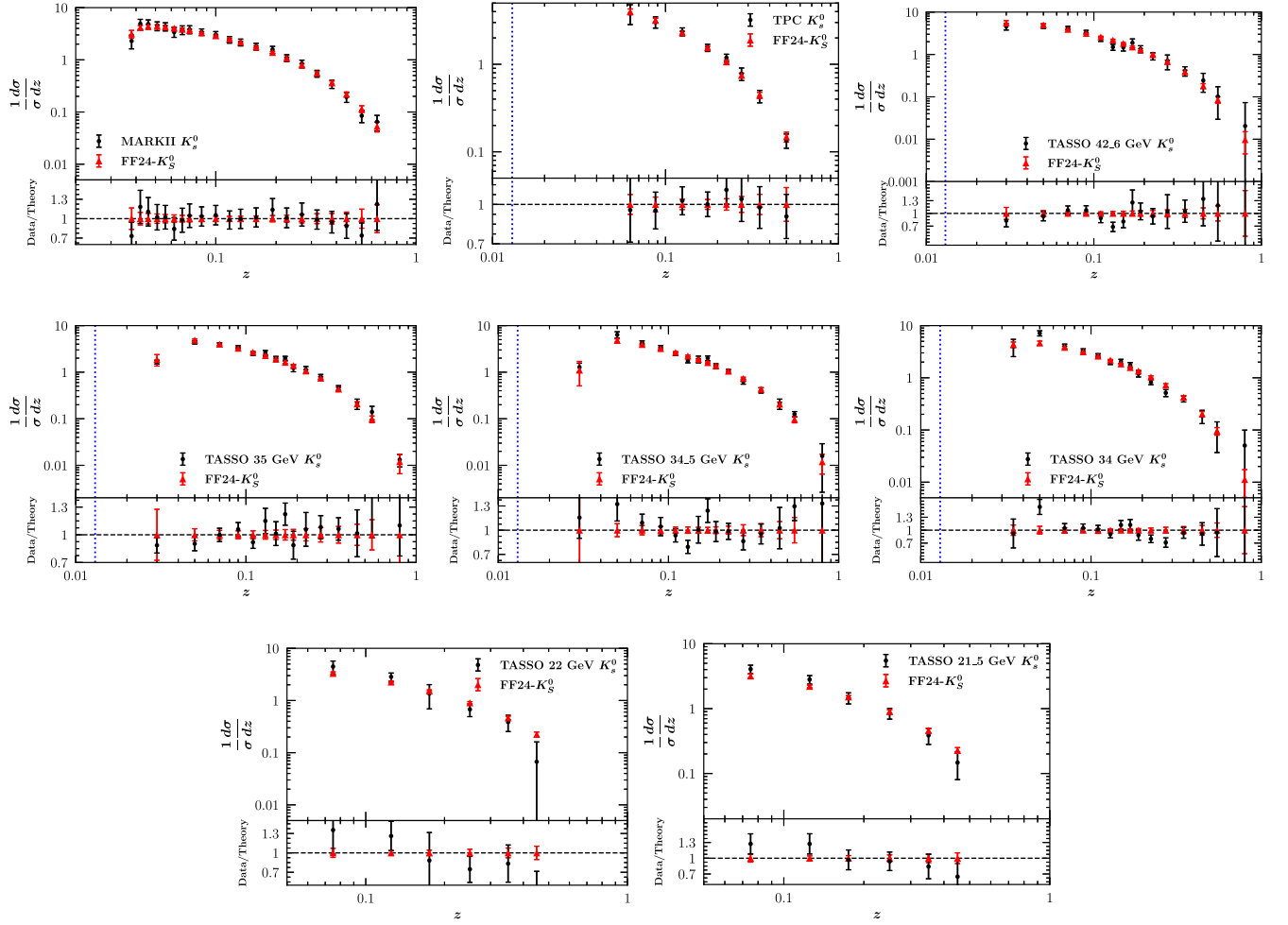
FIG. 4.   Same as Fig. 3 but this time for some other selected experimental data, including MARKII, TPC, TASSO42.6, TASSO35, TASSO34.5, TASSO34, TASSO22, TASSO21.5.

be concluded that smaller error bands are achieved, except for the case of d^+ and s^+ FFs.

In order to see how the BESIII data for K_S^0 production affect the determination of FFs, we compare in Fig. 8 data with predictions obtained from both the previous SAK20 FFs and the new FF24-K_S^0 FFs. We observe large differences between data and SAK20 predictions over the full range of z and for all energies. The theory predictions based on SAK20 FFs are not in good agreement with the BESIII data. In particular, the increase of cross-section predictions from SAK20 toward low values of z is not seen in the data. We believe that the main reason for this difference is that the SAK20 FFs had been extracted from high-energy SIA data and the predictions using QCD-backward evolution of FFs from high to low energies do not match the experimental results. We conclude that including BESIII data improve the fit for FFs in particular at low z.

In summary, our approach highlights two key improvements: First, the integration of the latest experimental data from BESIII, which enriches the dataset and enhances the reliability of our results. Second, the adoption of neural

networks in the fitting procedure introduces a novel technique to refine the extraction of FFs. This innovative combination of advanced methodologies contributes to a more accurate determination of K_S^0 FFs, offering improved precision and reliability for the prediction of measurements at future high-energy scattering experiments.

VI. SUMMARY AND OUTLOOK

In summary, the main goal of this paper is to introduce new sets of fragmentation functions for K_S^0, entitled FF24-K_S^0, obtained from a QCD analysis including NNLO corrections. Our analysis relies on extensive experimental data, incorporating measurements of K_S^0 production in the SIA process and including the most recent experimental data reported by the BESIII Collaboration.

The BESIII measurement covers collision energies spanning from $\sqrt{s} = 2.2324$ to $\sqrt{s} = 3.6710$ GeV below the range used in earlier FF fits. The findings presented in this study hold particular significance as they contribute
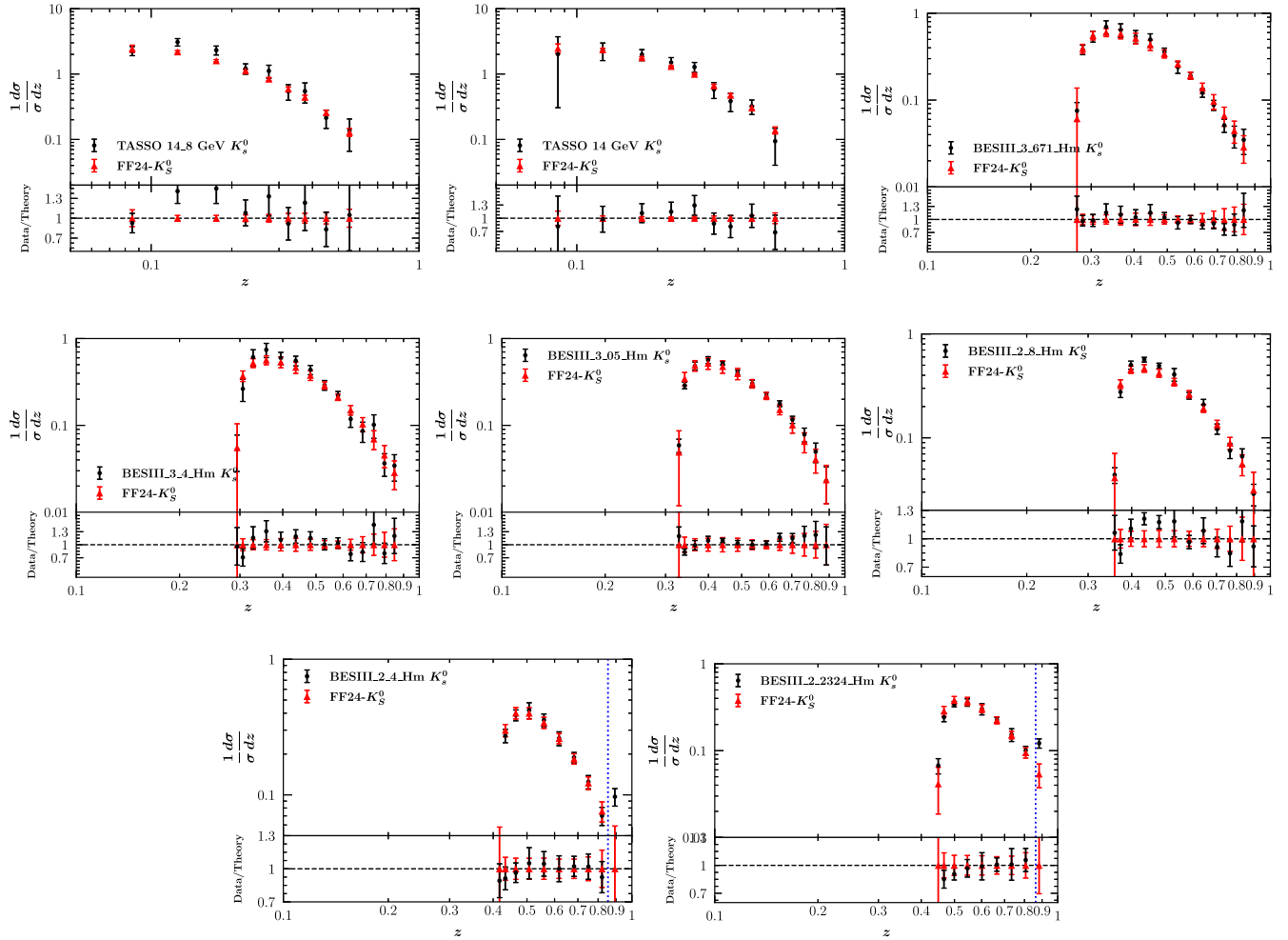
FIG. 5. Same as Fig. 3 but for some other selected experimental data including TASSO14.8, TASSO14, BESIII3.671, BESIII3.4, BESIII3.05, BESIII2.8, BESIII2.4, and BESIII2.2324.

valuable insight, especially in this new energy range below $\sqrt{s} < 10$ GeV where precise e^+e^- annihilation data have been scarce before. By analyzing normalized differential cross sections across this energy range, we have successfully addressed critical gaps in our understanding of K_S^0 hadron production.

Incorporating hadron mass corrections particularly in datasets with low values of energy and z, is crucial. In our analyses, we have applied K_S^0 mass corrections which allowed us to incorporate low-z data points, excluding only 8 data points with $z_{\min} = 0.013$. While small-z resummation is not explicitly addressed in our present analysis, we acknowledge its importance and plan to explore it in future investigations.

We have utilized neural networks to parameterize the fragmentation functions, aiming to minimize theoretical bias. The NN parameters are tuned to fit the SIA data. Our approach used the recent publicly available package MONTBLANC for FF parametrization, evolution, and SIA

production cross-section calculation. Moreover, we employ a Monte Carlo sampling method to propagate experimental uncertainties into the fitted FFs and determine uncertainties for both FFs and associated observables.

Both the overall χ^2 and the χ^2 values for individual datasets used in the fitting procedure are satisfactory. This is evident in the excellent agreement observed between the experimental data and the corresponding theoretical predictions. However, upon comparison with two other determinations, namely SAK20 and AKK08, some notable differences were identified in the resulting FF24-K_S^0 set. In this work, we focus exclusively on SIA observables to accurately determine the quark FFs of K_S^0. However, these measurements provide limited information about the gluon-to-hadron FFs since they are only accessible starting at NLO. Consequently, significant differences arise between our findings and those of other results available in the literature, such as AKK08, where K_S^0 production was investigated using also collider data. To gain a better
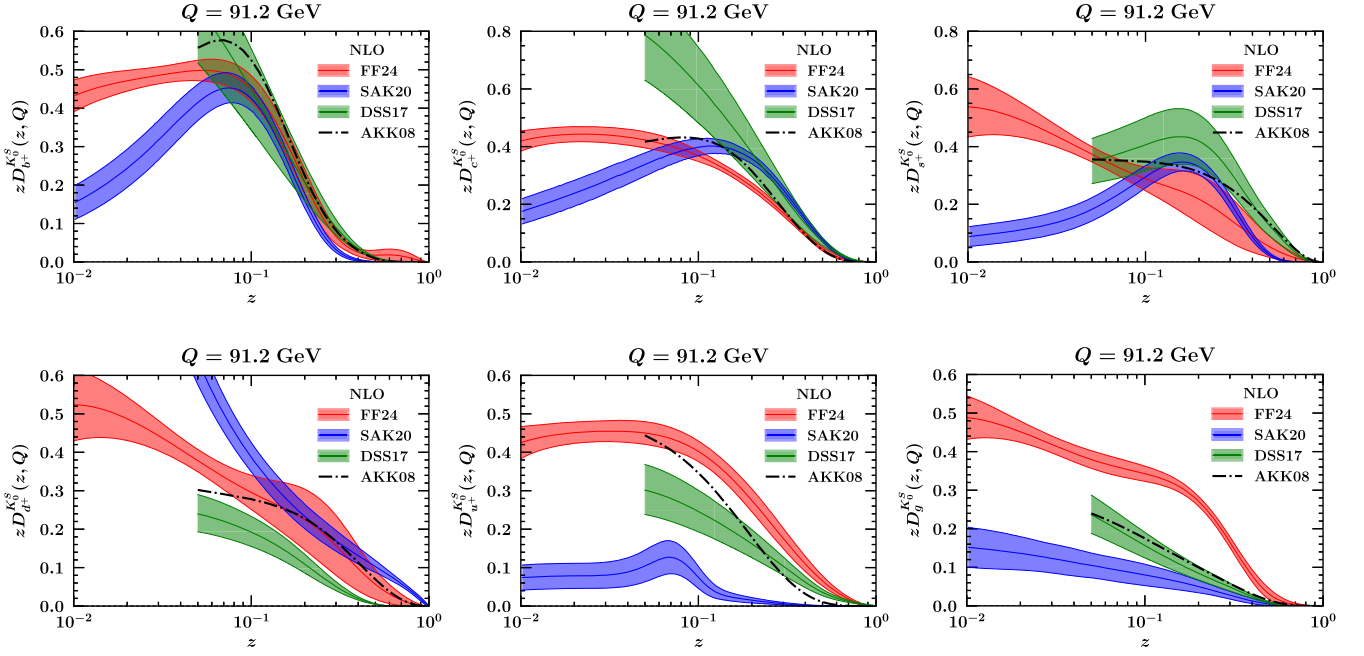
FIG. 6. The FF24-K_S^0 at NLO accuracy obtained for various partons at $\sqrt{s} = 91.2$ GeV. The shaded bands represent 1σ uncertainty estimates derived from the Monte Carlo method. Results from SAK20 [16], DSS17 [21], and AKK08 [20] at NLO accuracy, along with their 1σ error bands, are also included for comparison.

understanding of the gluonic contribution, we plan to extend our analysis to include data from the production of K_S^0 particles in proton collisions. Previous studies suggest that this will be particularly important for a better determination of the role of gluons in the overall picture.

The resulting FF24-K_S^0 sets at NLO and NNLO accuracy, along with their associated uncertainties, are made available in the standard LHAPDF format for broader utilization in the scientific community [52].
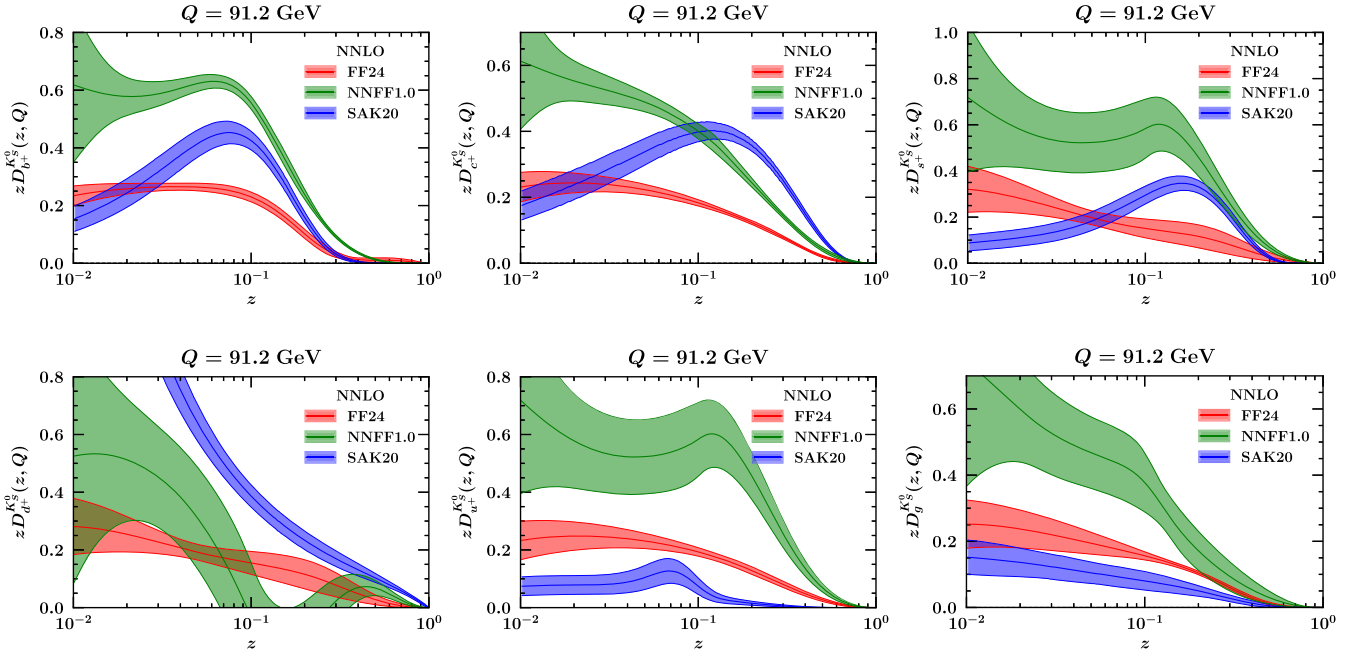
FIG. 7. Same as Fig. 6, but this time for the FF24-K_S^0 at NNLO accuracy. Results from SAK20 [16] and NNFF1.0 [22], along with their error bands at NNLO accuracy, are also included for comparison.
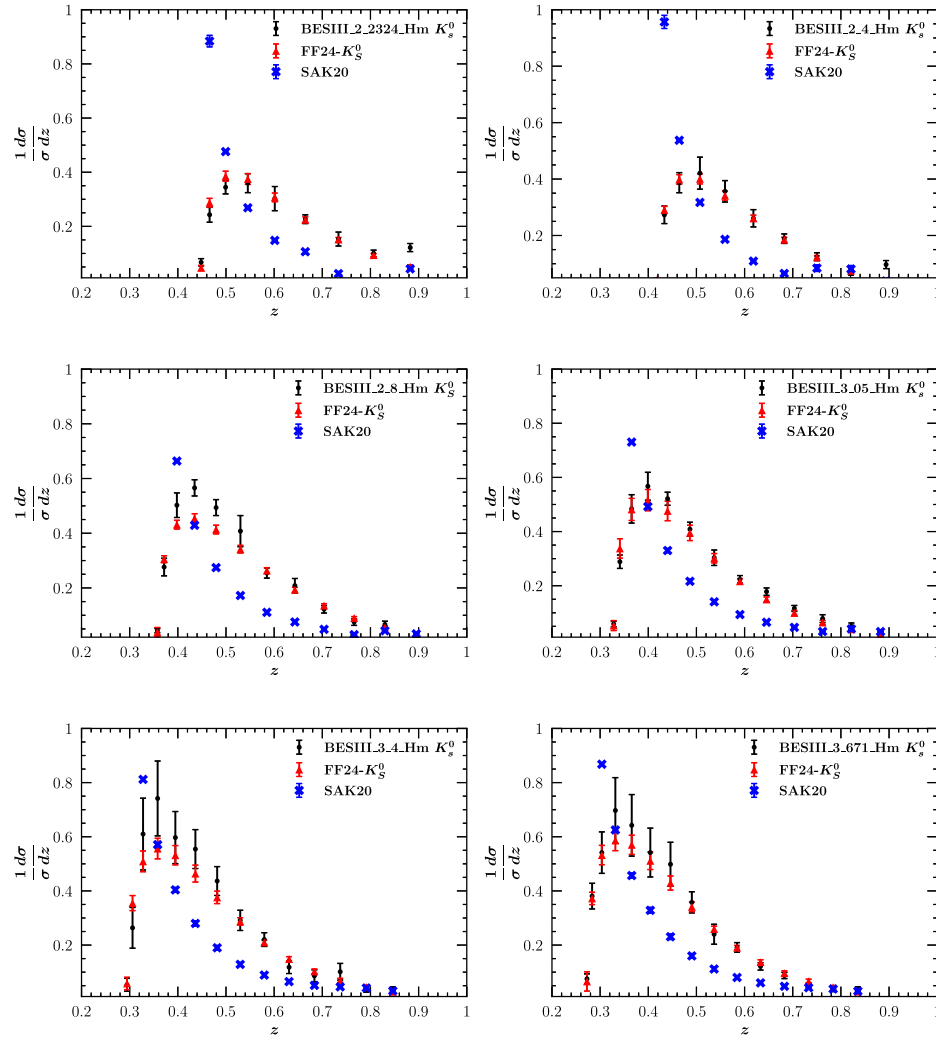
FIG. 8.   Comparison between the predictions for cross sections of K_S^0 production from SAK20 [16] and the present analysis at NLO accuracy and the measurements from the BESIII experiment.

ACKNOWLEDGMENTS

[1] J. C. Collins, D. E. Soper, and G. F. Sterman, Factorization of hard processes in QCD, Adv. Ser. Direct High Energy Phys. **5**, 1 (1989).

[2] A. A. Almasy, S. Moch, and A. Vogt, On the next-to-next-to-leading order evolution of flavour-singlet fragmentation functions, Nucl. Phys. **B854**, 133 (2012).

[3] A. Mitov, S. Moch, and A. Vogt, Next-to-next-to-leading order evolution of non-singlet fragmentation functions, Phys. Lett. B **638**, 61 (2006).

[4] M. Soleymaninia, H. Hashamipour, and H. Khanpour, Neural network QCD analysis of charged hadron fragmentation functions in the presence of SIDIS data, Phys. Rev. D **105**, 114018 (2022).

[5] R. Abdul Khalek, V. Bertone, A. Khoudli, and E. R. Nocera (MAP [Multi-dimensional Analyses of Partonic distributions] Collaboration), Pion and kaon fragmentation functions at next-to-next-to-leading order, Phys. Lett. B **834**, 137456 (2022).

[6] I. Borsa, R. Sassot, D. de Florian, M. Stratmann, and W. Vogelsang, Towards a global QCD analysis of fragmentation functions at next-to-next-to-leading order accuracy, Phys. Rev. Lett. **129**, 012002 (2022).

[7] E. Moffat, W. Melnitchouk, T. C. Rogers, and N. Sato (Jefferson Lab Angular Momentum (JAM) Collaboration), Simultaneous Monte Carlo analysis of parton densities and fragmentation functions, Phys. Rev. D **104**, 016015 (2021).

[8] A. Abada *et al.* (FCC Collaboration), FCC physics opportunities: Future circular collider conceptual design report volume 1, Eur. Phys. J. C **79**, 474 (2019).

[9] A. Abada *et al.* (FCC Collaboration), HE-LHC: The high-energy large hadron collider: Future circular collider conceptual design report volume 4, Eur. Phys. J. Special Topics **228**, 1109 (2019).

[10] R. Abdul Khalek, A. Accardi, J. Adam, D. Adamiak, W. Akers, M. Albaladejo, A. Al-bataineh, M. G. Alexeev, F. Ameli, P. Antonioli *et al.*, Science requirements and detector concepts for the electron-ion collider: EIC Yellow Report, Nucl. Phys. **A1026**, 122447 (2022).

[11] I. Borsa, G. Lucero, R. Sassot, E. C. Aschenauer, and A. S. Nunes, Revisiting helicity parton distributions at a future electron-ion collider, Phys. Rev. D **102**, 094018 (2020).

[12] M. Klasen and H. Paukkunen, Nuclear PDFs after the first decade of LHC data, arXiv:2311.00450.

[13] G. Aad *et al.* (ATLAS Collaboration), Measurement of K_S^0 and Λ^0 production in $t\bar{t}$ dileptonic events in pp collisions at $\sqrt{s} = 7$ TeV with the ATLAS detector, Eur. Phys. J. C **79**, 1017 (2019).

[14] G. Aad *et al.* (ATLAS Collaboration), Kshort and Λ production in pp interactions at $\sqrt{s} = 0.9$ and 7 TeV measured with the ATLAS detector at the LHC, Phys. Rev. D **85**, 012001 (2012).

[15] D. Acosta *et al.* (CDF Collaboration), K_S^0 and Λ^0 production studies in $p\bar{p}$ collisions at $\sqrt{s} = 1800$-GeV and 630-GeV, Phys. Rev. D **72**, 052001 (2005).

[16] M. Soleymaninia, H. Abdolmaleki, and H. Khanpour, First NNLO fragmentation functions of K_S^0 and $\Lambda/\bar{\Lambda}$ and their uncertainties in the presence of hadron mass corrections, Phys. Rev. D **102**, 114029 (2020).

[17] J. Binnewies, B. A. Kniehl, and G. Kramer, Neutral kaon production in e^+e^-, ep and pp^- collisions at next-to-leading order, Phys. Rev. D **53**, 3573 (1996).

[18] C. Bourrely and J. Soffer, Statistical approach for unpolarized fragmentation functions for the octet baryons, Phys. Rev. D **68**, 014003 (2003).

[19] S. Albino, B. A. Kniehl, and G. Kramer, Fragmentation functions for K_S^0 and Λ with complete quark flavor separation, Nucl. Phys. **B734**, 50 (2006).

[20] S. Albino, B. A. Kniehl, and G. Kramer, AKK update: Improvements from new theoretical input and experimental data, Nucl. Phys. **B803**, 42 (2008).

[21] D. de Florian, M. Epele, R. J. Hernandez-Pinto, R. Sassot, and M. Stratmann, Parton-to-kaon fragmentation revisited, Phys. Rev. D **95**, 094019 (2017).

[22] V. Bertone, S. Carrazza, N. P. Hartland, E. R. Nocera, and J. Rojo (NNPDF Collaboration), A determination of the fragmentation functions of pions, kaons, and protons with faithful uncertainties, Eur. Phys. J. C **77**, 516 (2017).

[23] M. Ablikim *et al.* (BESIII Collaboration), Measurements of normalized differential cross sections of inclusive π^0 and K_S^0 production in e^+e^- annihilation at energies from 2.2324 to 3.6710 GeV, Phys. Rev. Lett. **130**, 231901 (2023).

[24] R. A. Khalek, V. Bertone, and E. R. Nocera, Determination of unpolarized pion fragmentation functions using semi-inclusive deep-inelastic-scattering data, Phys. Rev. D **104**, 034007 (2021).

[25] R. D. Ball *et al.* (NNPDF Collaboration), Parton distributions from high-precision collider data, Eur. Phys. J. C **77**, 663 (2017).

[26] https://github.com/MapCollaboration/MontBlanc.

[27] M. Althoff *et al.* (TASSO Collaboration), A detailed study of strange particle production in e^+e^- annihilation at high-energy, Z. Phys. C **27**, 27 (1985).

[28] W. Braunschweig *et al.* (TASSO Collaboration), Strange meson production in e^+e^- annihilation, Z. Phys. C **47**, 167 (1990).

[29] M. Derrick *et al.*, Hadron production in e^+e^- annihilation at $\sqrt{s} = 29$-GeV, Phys. Rev. D **35**, 2639 (1987).

[30] H. Aihara *et al.* (TPC/Two Gamma Collaboration), K^{*0} and K_s^0 meson production in e^+e^- annihilations at 29-GeV, Phys. Rev. Lett. **53**, 2378 (1984).

[31] H. Schellman *et al.*, Measurement of $K^\pm$ and K^0 inclusive rates in e^+e^- annihilation at 29-GeV, Phys. Rev. D **31**, 3013 (1985).

[32] H. J. Behrend *et al.* (CELLO Collaboration), Inclusive strange particle production in e^+e^- annihilation, Z. Phys. C **46**, 397 (1990).

[33] R. Itoh *et al.* (TOPAZ Collaboration), Measurement of inclusive particle spectra and test of MLLA prediction in e^+e^- annihilation at $s = 58$-GeV, Phys. Lett. B **345**, 335 (1995).

[34] R. Barate *et al.* (ALEPH Collaboration), Studies of quantum chromodynamics with the ALEPH detector, Phys. Rep. **294**, 1 (1998).

[35] P. Abreu *et al.* (DELPHI Collaboration), Production characteristics of K^0 and light meson resonances in hadronic decays of the Z^0, Z. Phys. C **65**, 587 (1995).

[36] G. Abbiendi *et al.* (OPAL Collaboration), Leading particle production in light flavor jets, Eur. Phys. J. C **16**, 407 (2000).

[37] K. Abe *et al.* (SLD Collaboration), Production of π^+, K^+, K^0, K^{*0}, φ, p and Λ^0 in hadronic Z^0 decays, Phys. Rev. D **59**, 052001 (1999).

[38] P. Abreu *et al.* (DELPHI Collaboration), Charged and identified particles in the hadronic decay of W bosons and in $e^+e^- \rightarrow q\bar{q}$ from 130-GeV to 200-GeV, Eur. Phys. J. C **18**, 203 (2000); Eur. Phys. J. C **25**, 493(E) (2002).

[39] A. Mitov and S. O. Moch, QCD corrections to semi-inclusive hadron production in electron-positron annihilation at two loops, Nucl. Phys. **B751**, 18 (2006).

[40] Y. L. Dokshitzer, Calculation of the structure functions for deep inelastic scattering and e^+e^- annihilation by perturbation theory in quantum chromodynamics., Sov. Phys. JETP **46**, 641 (1977).

[41] S. Agarwal, K. Mierle *et al.*, Ceres solver, http://ceres-solver .org.

[42] https://github.com/rabah-khalek/NNAD.

[43] V. Bertone, APFEL++: A new PDF evolution library in C++, *Proc. Sci.*, DIS2017 (2018) 201 [arXiv:1708 .00911].

[44] S. Forte, L. Garrido, J. I. Latorre, and A. Piccione, Neural network parametrization of deep-inelastic structure functions, J. High Energy Phys. 05 (2002) 062.

[45] B. C. Csáji *et al.*, Approximation with artificial neural networks, M.Sc thesis, Faculty of Sciences, Etvs Lornd University, Hungary, 2001.

[46] R. A. Khalek, Exploring the substructure of nucleons and nuclei with machine learning, arXiv:2110.01924.

[47] M. Soleymaninia, H. Hashamipour, H. Khanpour, and H. Spiesberger, Fragmentation functions for Ξ^-/Ξ^+ using neural networks, Nucl. Phys. **A1029**, 122564 (2023).

[48] H. Moutarde, P. Sznajder, and J. Wagner, Unbiased determination of DVCS Compton form factors, Eur. Phys. J. C **79**, 614 (2019).

[49] N. Sato, J. J. Ethier, W. Melnitchouk, M. Hirai, S. Kumano, and A. Accardi, First Monte Carlo analysis of fragmentation functions from single-inclusive e^+e^- annihilation, Phys. Rev. D **94**, 114004 (2016).

[50] R. Abdul Khalek, J. J. Ethier, and J. Rojo (NNPDF Collaboration), Nuclear parton distributions from lepton-nucleus scattering and the impact of an electron-ion collider, Eur. Phys. J. C **79**, 471 (2019).

[51] N. Sato, W. Melnitchouk, S. E. Kuhn, J. J. Ethier, and A. Accardi (Jefferson Lab Angular Momentum Collaboration), Iterative Monte Carlo analysis of spin-dependent parton distributions, Phys. Rev. D **93**, 074005 (2016).

[52] https://github.com/hashamipour/FF24_K0S_LHAPDF.